A&A 478, 543–551 (2008)
DOI: 10.1051/0004-6361:20078293

Astronomy & Astrophysics

Axi-symmetric models of B[e] supergiants

I. The effective temperature and mass-loss dependence of the hydrogen and helium ionization structure

J. Zsargó[1], D. J. Hillier[1], and L. N. Georgiev[2]

[1] Dept. of Physics and Astronomy, University of Pittsburgh, 3941 O'Hara St., Pittsburgh, PA 15260, USA
e-mail: jzsargo@astro.phyast.pitt.edu
[2] Instituto de Astronomia, Universidad Nacional Autonoma de Mexico (UNAM), CD. Universitaria, Apartado Postal 70-264, 04510, México DF, México

Received 17 July 2007 / Accepted 21 November 2007

ABSTRACT

Aims. We calculate the hydrogen and helium ionization in B[e] envelopes and explore their dependence on mass-loss and effective temperature. We also present simulated observations of the Hα emission line and the C IV $\lambda\lambda$1550 doublet, and study their behavior. This paper reports our first results in an ongoing study of B[e] supergiants, and provides a glimpse on the ionization of the most important elements in self-consistent numerical simulations.
Methods. Our newly developed 2D stellar atmosphere code, ASTAROTH, was used for the numerical simulations. The code self-consistently solves for the continuum radiation, non-LTE level populations, and electron temperature in axi-symmetric stellar envelopes. Observed profiles were calculated by an auxiliary program developed separately from ASTAROTH.
Results. In all but one of our models, H remained fully ionized – only for $\dot{M} > 10^{-5}$ $M_\odot$ yr^{-1} and $T_{\rm eff} \leq 18\,000$ K did we obtain a neutral H disk, and then only for radii beyond 3 R_*. Due to ionizations from excited states it is much more difficult to get a H neutral disk than indicated by previous analytical calculations. Near the poles, the ionization is high in all models, while helium recombined in the equatorial regions for all but our lowest mass-loss rate (10^{-6} $M_\odot$ yr^{-1}). Although the model parameters were not adjusted to provide fits to any particular star, the theoretical profiles show some features seen in the profiles of R126. These include the partially resolved double peaked profile of Hα, and the weak emission associated with the UV C IV resonance line.

Key words. radiative transfer – atomic processes – stars: early-type – stars: winds, outflows

1. Introduction

Massive stars are very important constituents of the Universe despite their low share of galactic masses. They are the primary sources of elements heavier than Li and power the internal evolution of galaxies by their radiation, winds, and explosions. Many of these stars, and their immediate environment, cannot be fully understood in the context of plane-parallel or spherical models, and their multidimensional nature has to be taken into account if their evolution or physical state is to be adequately described. The origin of their asphericity is either fast rotation, the presence of a dynamically important magnetic field, or their interaction with a companion.

Three groups of such stars are particularly relevant for this paper. These are the classical Be stars, the Luminous Blue Variables (LBV), and the B[e] supergiants (sgB[e]), all of which share many similar characteristics. The 2D or 3D nature of these objects was recognized through both observations and theoretical calculations. For example, the presence of disks around classical Be stars was inferred from line modeling and polarimetric studies (Poeckert & Marlborough 1978a,b), and has been confirmed by interferometric observations (Stee et al. 1995; Quirrenbach et al. 1997). Similarly, a growing body of evidence suggests that the LBV phenomenon includes 2D or 3D processes. For example, η Car is a binary (Damineli et al. 2000) and the Homunculus nebula around it is the most cited example of a bipolar outflow. The aspherical envelope of η Car is not unique among LBVs; Groh et al. (2006) found that AG Car is a fast rotator, and hence may have a latitude dependent wind. The relevance of the binarity and fast rotation in the LBV phenomenon in general is not yet clear and is the subject of vigorous research (e.g., Martin et al. 2006; Nielsen et al. 2007).

B[e] stars, or rather the stars that show B[e] phenomenon (Lamers et al. 1998), are characterized by strong broad H Balmer emission lines (as are the classical Be stars) and by the presence of narrow permitted and forbidden emission lines from low-ionization species, like Fe II, [Fe II], or [O I]. B[e] stars also show strong near/mid-IR excess that is attributed to hot cirumstellar dust. Interested readers should refer to Zickgraf et al. (1985, 1986, 1992); Miroshnichenko et al. (2005) and references therein for further information on the B[e] phenomenon. A particularly interesting subclass of the B[e] stars are the sgB[e]-s (Lamers et al. 1998). These are single B supergiants that show the B[e] phenomenon and are located near the Humphreys-Davidson limit (Humphreys & Davidson 1979, 1984). Their location on the HR diagram may suggest a link to the more massive LBVs or, alternatively, they may represent a second evolutionary path between Of and Wolf-Rayet (W-R) stars (Schulte-Ladbeck 1998; Zickgraf 1998).

The envelope of sgB[e] stars is thought to be latitude dependent, with a normal B supergiant wind at the pole and a dense and slowly moving equatorial flow (Zickgraf et al. 1985, 1986). Polarimetric observations by Magalhaes (1992); Oudmaijer et al. (1998); Melgarejo et al. (2001) revealed that sgB[e]-s have strong intrinsic polarization consistent with this

picture. The most widely accepted theory for the bi-modal nature of the envelope is the rotationally induced bi-stability. Around $T_{\rm eff}$ = 20 000−25 000 K the characteristics of the line-driven wind abruptly change due to the recombination of Fe IV to Fe III (Pauldrach & Puls 1990; Lamers & Pauldrach 1991; Vink et al. 1999). If the sgB[e] stars are fast rotators, as suggested, the ensuing gravity-darkening can place the equatorial and polar regions on the opposite sides of the bistability, hence providing a mechanism to produce the bi-modal envelope. However, the bi-stability model is not without its weaknesses. For example, gravity darkening reduces the flux at the equator, potentially inhibiting any equatorial enhanced mass-flux. It is also difficult to maintain multiple scattering in the equator when the photons can easily escape in the polar direction. (see discussion in Sect. 7). Consequently, other sgB[e] models have been proposed, like the presence of a Keplerian disk similar to those around classical Be stars. Further, disk winds as proposed by Oudmaijer et al. (1998), the traditional wind compressed disk model of Bjorkman & Cassinelli (1993), and even the magnetically confined disk models (ud-Doula & Owocki 2002; Owocki & ud-Doula 2004) cannot be excluded. So far, theoretical efforts have primarily focused on understanding the hydrodynamic structure in the context of the bi-stability model, and trying to incorporate the bi-stability jump into the Castor et al. (1975) formalism (e.g., Pelupessy et al. 2000; Curé et al. 2005).

There have only been a few efforts to understand the ionization structure of the wind and to perform spectral analysis of B[e] stars. Semi-analytical calculations of hydrogen and helium ionization were done by Kraus & Lamers (2003) and Kraus (2006), and they found the equatorial disk essentially neutral in these species all the way down to the stellar surface. Porter (2003) attempted to reproduce the optical to infra-red continuum of R 126 (prototype sgB[e] in the LMC) by using bi-stability and Keplerian viscous disk models. Both of them reproduced the optical and near-IR emission, but they failed to account for the dust emission by an order of magnitude. Recently, Kraus et al. (2007) proposed that the dust and optical/near-IR continuum emission can be reconciled if the free-free and bound-free emission originates from the polar wind rather than the equatorial disk.

A self-consistent spectral analysis of a stellar envelope needs to solve the coupled equations for the radiation field and level populations. Obviously, this is a very difficult task in a non-LTE 2D or 3D envelope and compromises and simplifications are inevitable. Kraus & Lamers (2003) and Kraus (2006), for example, used a simplified radiative transfer, limited their analysis to optically thin or optically thick cases, and neglected ionization from excited levels; all of these can potentially have serious effects on the resulting ionization structure. While significant insights can be gained by simple calculations, one needs numerical simulations for a fully self-consistent spectral analysis.

To provide a tool for such studies of Be/B[e] stars, binaries, and LBVs, we have been developing a code for axi-symmetric models. So far, only basic tests and code verification were performed (Georgiev et al. 2006; Zsargó et al. 2006), but we have now reached the point where scientifically meaningful simulations can be performed. The ionization structure of hydrogen and helium in axi-symmetric sgB[e] envelopes offers such an opportunity. The details of the program are discussed in Georgiev et al. (2006) and Zsargó et al. (2006) so we only briefly describe it in Sect. 2. The hydrodynamic structures and the atomic models that are used in our simulations are discussed in Sect. 3; computational issues are discussed in Sect. 4; and our results are presented in Sect. 5. Simulated observations are shown in Sect. 6, and we draw our conclusions in Sects. 7 and 8.

2. The code

Our C++ code, ASTAROTH, was developed for simulations of stellar envelopes. However, it is flexible enough to be applied to any hot axi-symmetrical object with velocity gradients (including extragalactic objects, like AGN-s).

The non-LTE level populations, the radiation field, and the electron temperature are calculated by simultaneously solving the equations of statistical equilibrium, radiative transfer, and energy conservation. The short-characteristic method (see e.g., Mihalas et al. 1978; Kunasz & Auer 1988; Busche & Hillier 2000) is used to treat the continuum radiation transfer while bound-bound transitions are treated, for simplicity, by the Sobolev approximation. The simultaneous solution of the equations is found by an approximate lambda iteration (Rybicki & Hummer 1991, 1992). The code has been tested by solving 2D pure scattering problems with grey opacity, as well as reproducing spherical symmetric models of CMFGEN (Hillier & Miller 1998), a well-established code in stellar studies. In these tests, the new code reproduced the reference results within a few percent (see, Zsargó et al. 2006; Georgiev et al. 2006).

3. Models

To simulate the hydrodynamical structure of a sgB[e] atmosphere we followed the approach of Kraus & Lamers (2003), but relaxed two of their simplifications. We used a β-law (Castor et al. 1975) to describe the radial velocity and allowed for a varying electron temperature. Our velocity field was still simplified; only a latitude dependent radial velocity was included and the azimuthal and latitudinal velocities were set to zero. To simulate the bi-modal wind, we described the radial velocity and the mass-loss per unit solid angle by

$$V_r(R,\theta) = V_\infty(\theta=0)\cdot 10^{b_{\rm v}\,\sin^s\theta}\cdot\left(1-\frac{R_*}{R}\right)^\beta \tag{1}$$

and

$$\frac{\partial^2 M}{\partial t\partial\Omega}(\theta) = \frac{\partial^2 M}{\partial t\partial\Omega}(\theta=0)\cdot 10^{b_{\rm m}\,\sin^s\theta}, \tag{2}$$

respectively. The parameters R and θ are the traditional polar coordinates, and s controls the thickness of the equatorial disk; the larger it gets the thinner the disk. In our simulations s was set to 10, unlike in Kraus & Lamers (2003) where 10 and 100 were used. In these initial calculations we avoided the higher values because of the need to have a much finer spatial grid which would have substantially increased the computational effort. In a future, detailed analysis of sgB[e]s, the effects of varying disk thickness will need to be explored.

Using Eq. (2) and assuming top-bottom symmetry, the total mass-loss rate can be calculated by

$$\dot{M} = 4\pi\cdot\int_0^{\frac{\pi}{2}}\frac{\partial^2 M}{\partial t\partial\Omega}(\theta)\cdot\sin\theta\,{\rm d}\theta. \tag{3}$$

Also, because all non-radial velocities are zero, the gas density in the wind, $\rho(r,\theta)$ is given by

$$\rho(R,\theta) = \frac{\partial^2 M}{\partial t\partial\Omega}(\theta)\cdot\frac{1}{R^2 V_r(R,\theta)}. \tag{4}$$

In our models we used $b_{\rm v} = -2$ and $b_{\rm m} = 1$ which resulted in a 3 order of magnitude density enhancement and a 2 order of magnitude velocity decrease between the pole and the disk (see

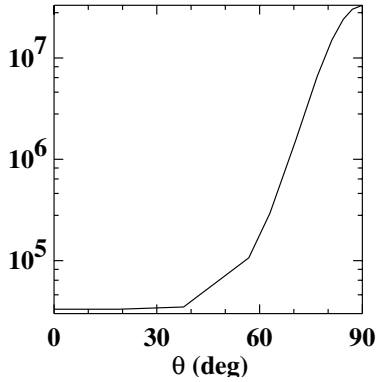

Fig. 1. The density as a function of latitude at $R = 100\ R_*$ in our models A and B (see Table 1). Note that the density scale is logarithmic. The density distribution for models C and D is similar in shape, but the values are 10 times greater.

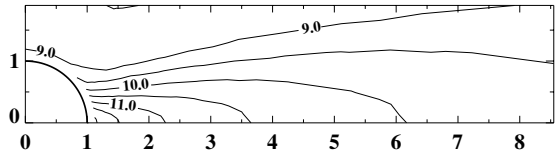

Fig. 2. A meridional snapshot of the logarithmic hydrogen density near the star for models A and B. The pole is toward the top of the page and the equator is horizontal. The envelope is axi-symmetric around the pole and top-bottom symmetric around the equator. The units are in stellar radius and the thick circle at the center represents the surface of the star. A similar snapshot for models C and D would look identical except with larger density values. Note, that the open contour lines near the stellar surface are artifacts of omitting the region $R < 1.1\ R_*$ from the plot which was done for clarity.

Sect. 7 for discussion on the validity of Sobolev approximation in the disk). The 2D density structure is displayed in Figs. 1 and 2. The bi-modal structure of the wind is apparent with 3 order of magnitude difference between the pole ($\theta = 0°$) and the equator ($\theta = 90°$).

There is a significant difference between our approach and that of Kraus & Lamers (2003). They did not deal with the photosphere, and used Kurucz (1979) spectra to simulate the stellar radiation field. ASTAROTH, similarly to CMFGEN, solves for the unknown level populations and ionization structure, and calculates spectra for both the photosphere and the wind. It uses the same methods as CMFGEN (Hillier & Miller 1998) to create an approximate hydrostatic photosphere. In brief, the wind follows a simple beta-like velocity law (Castor et al. 1975), and for this work starts at a radius $R_{\rm phot}$ defined by $V_r(R_{\rm phot}, \theta) = 1\ {\rm km\,s^{-1}}$. Below this radius the density follows an exponential law and the velocity is set by the continuity equation for the given mass-loss rate. The value of $R_{\rm phot}$ is latitude dependent in the models presented here, but it was always nearly R_* (<1−2% difference).

For the stellar parameters, listed in Table 1, we chose values that are broadly representative of the most luminous sgB[e]-s (see, Zickgraf et al. 1985, 1986) and some less luminous LBVs (e.g., P Cygni, Pauldrach & Puls 1990; Drew 1985). The mass-loss range covers the upper end of the range used in Kraus & Lamers (2003) and includes their baseline models (models A, C, and F in Kraus & Lamers 2003). The suspected mass-loss rate of R 126 (~$4 \times 10^{-5}\ M_\odot\ {\rm yr^{-1}}$, Bjorkman 1998) is also near our mass-loss range. We vary the effective temperature between $T_{\rm eff} \sim 22\,500$ K ($L = 1.5 \times 10^6\ L_\odot$), that of R 126, to $T_{\rm eff} \sim 18\,000$ K ($L = 6 \times 10^5\ L_\odot$) which approximately covers the sgB[e] temperature range in the Magellanic Clouds (see, Zickgraf et al. 1985, 1986).

Table 1. Description of the models.

Model	A	B	C	D
M_*	$30\ M_\odot$			
R_*	$82\ R_\odot$			
$T_{\rm eff}$	22 500 K	18 000 K	22 500 K	18 000 K
$\frac{\partial^2 M}{\partial t \partial \Omega}(\theta = 0)$	$8 \times 10^{-8}\ \frac{M_\odot}{\rm yr\ str}$		$8 \times 10^{-7}\ \frac{M_\odot}{\rm yr\ str}$	
$\frac{\partial^2 M}{\partial t \partial \Omega}(\theta = \frac{\pi}{2})$	$8 \times 10^{-7}\ \frac{M_\odot}{\rm yr\ str}$		$8 \times 10^{-6}\ \frac{M_\odot}{\rm yr\ str}$	
$\dot{M}$	$3.3 \times 10^{-6}\ M_\odot\ {\rm yr^{-1}}$		$3.3 \times 10^{-5}\ M_\odot\ {\rm yr^{-1}}$	
$V_\infty(\theta = 0)$	$2000\ {\rm km\,s^{-1}}$			
$V_\infty(\theta = \frac{\pi}{2})$	$20\ {\rm km\,s^{-1}}$			
β^a	0.8			

[a] Power for the standard β velocity law (Castor et al. 1975).

Table 2. Atomic model.

Specie	Number of Levels
H I	20
H II	1
He I	11
He II	20
He III	1
C II	9
C III	10
C IV	5
C V	1

Finally, the atomic model is presented in Table 2. We used essentially H/He atmospheres with a fairly large number of levels included. A few levels and ionization states of carbon were also included to achieve more realistic heating and cooling terms. The fractional (number) abundances of He and C was 0.1 and 9.82×10^{-4}, respectively. The later number represents the net abundance of CNO elements.

4. Computational issues

Previous works on stellar winds and sgB[e] stars (e.g., Kraus & Lamers 2003) have found that ionization changes can occur suddenly, in the form of ionization fronts. One of our main concerns was, therefore, whether our spatial grid would adequately resolve a potential 2D ionization front in our simulations. The standard grid included 60−80 depth points and ~10 latitudes, both of them spaced semi-irregularly with the limitation that all latitude must have the same radial grid. The only problem we encountered was the sharp hydrogen recombination front that occurred in model D, and the spatial grid had to be adjusted by hand to better resolve the front (adaptive gridding capability is not yet included in ASTAROTH). Otherwise the standard grid was adequate for our models. Simulations on a denser grid with 120 depth and 20 latitude points revealed no qualitative changes in the populations and temperatures.

The convergence was also sometimes slowed by oscillations in the low radiation field/high density equatorial disk. As the statistical equilibrium and energy conservation equations are highly nonlinear in the populations, radiation field, and electron temperature, solution techniques can provide oscillating solutions. Often the oscillations arose at depths, and in populations, where changes would have a negligible influence on the emergent

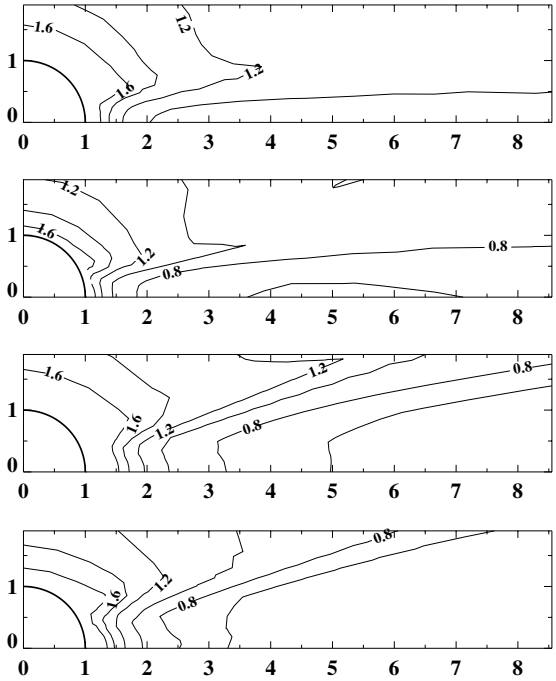

Fig. 3. The temperature structure near the star in models A, B, C, and D (*top to bottom*). The layout of the plots is the same as that of Fig. 2. The contour levels are from 6000 K to 16 000 K in 2000 K increments and shown in 10 000 K units.

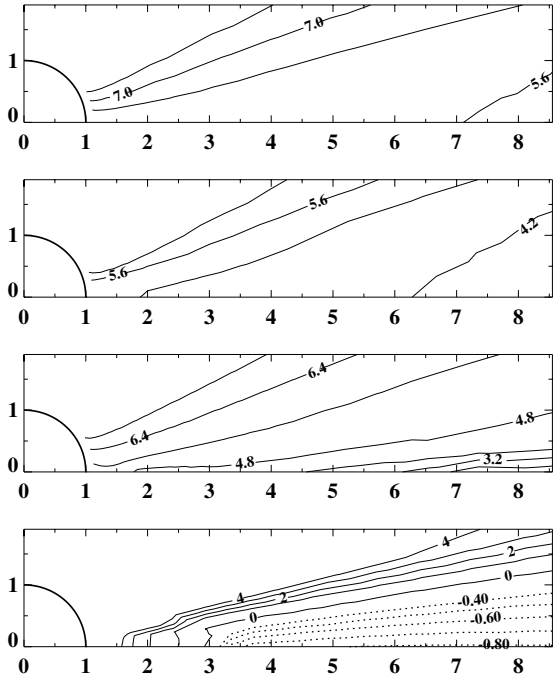

Fig. 4. The $\log\left(\frac{N_{\rm H\,II}}{N_{\rm H\,I}}\right)$ contours for models A, B, C, and D (*top to bottom*). The layout of the figures is the same as that of Fig. 2. The thin solid lines represent ratios above 0 (ionized H) and the thick dotted lines show neutral regions. Note, that the lower the ratio the more neutral the hydrogen is! The spacing between levels is different from figure to figure and between neutral and ionized regions.

spectrum. Unfortunately, since we currently use a stopping criterion based on the maximum population change, such oscillations can greatly increase the total computational effort. To dampen the oscillations we linearized the statistical equilibrium equations with populations averaged over several previous iteration cycles. Switching to linear interpolations of quantities, instead of the standard cubic or parabolic approximations, also improved the convergence. The linear interpolation is an extremely well-behaved and stable approximation and it would be the preferred method if it provided the necessary accuracy. Unfortunately, this is not the case for spatial grids that are practical for ASTAROTH simulations; therefore, linear interpolation was limited to grid-points immediately around the trouble spot.

5. Ionization and temperature structure

Figures 3–5 show the electron temperature, hydrogen, and helium ionization structures, respectively, in our model envelopes.

5.1. Electron temperature

The electron temperature varies between ∼100 000 K to ∼20 000 K in the inner hydrostatic atmosphere (not shown in Fig. 3), and it was a few 1000 K in the outer envelope. The behavior of $T_{\rm e}$ in the wind is similar, as expected, for all models – the equator is cooler than the pole at the same radius. The effect of the lower luminosity in models B and D is a shift of the overall structure closer to the stellar surface (see Fig. 3), while increasing the mass-loss results in a thicker cool disk. It is immediately obvious from Fig. 3 that models C and D have a bulkier and wider "disk" than models A and B.

The temperature in our models is too hot for dust formation. Nowhere in our models the temperature falls below ∼1500 K which is the upper limit for dust formation (Porter 2003). We cannot conclude, however, that dust is formed beyond $R > 100{-}200\ R_*$ (the outer boundary of our models) because of the relative simplicity of our models and the neglect of adiabatic cooling in our simulations. We will address this question in follow-up studies with models constrained by the observations of individual stars.

5.2. Hydrogen ionization

Figure 4 shows the ionized to neutral H ratio in logarithmic scale where neutral H means the total population of all H I levels. It was very difficult to display the wide range of ionization levels occurring in our models. Since there were orders of magnitude differences even within a single model, we opted for using a separate set of contour levels for each model.

The hydrogen ionization shows latitudinal variations similar to those of the temperature. The equatorial region is more neutral than the pole in all models, and the lower the effective temperature or higher the mass-loss the more neutral the inner envelope. In only one model, model D, does a neutral H disk form, and then only beyond ∼3 R_*. This contradicts the result of Kraus & Lamers (2003) who found predominantly neutral hydrogen disks, even nearly at the surface, for very similar models. In our models A−C the neutral hydrogen is negligible compared to H II (inside 10 R_*), although there is a tendency for the neutral hydrogen fraction to rise at larger radii. The high level of ionization prevails even if the effective temperature is lowered (model B) or the mass-loss rate is increased (model C). Only the combined effect of the two (model D) produced a neutral hydrogen disk. We will further discuss the differences between our results and those of Kraus & Lamers (2003) in Sect. 7.

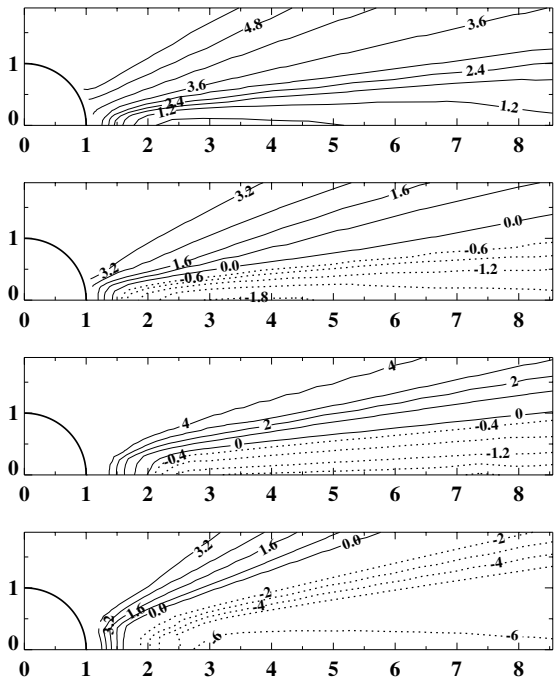

Fig. 5. The $\log\left(\frac{N_{\rm He\ III}+N_{\rm He\ II}}{N_{\rm He\ I}}\right)$ contours for models A, B, C, and D (*top to bottom*). The layout of the plots and the definitions of the contour lines are the same as those of Figs. 2 and 4, respectively.

5.3. Helium ionization

Figure 5 shows the logarithm of the ionized to neutral He ratio. Ionized He means the total population of all He II and He III levels. The ionization level of helium is markedly lower than that of hydrogen, a result to be expected given the low effective temperatures which were adopted. As opposed to H, He forms a neutral disk in all but one of our models – in model A, only an enhancement of neutral helium occurs in the equatorial region. The neutral disks show characteristics similar to those of the temperature distribution or hydrogen ionization; e.g, lowering $T_{\rm eff}$ results in an inward shift of the neutral regions as seen in the last two panels of Fig. 5. Higher mass-loss causes the neutral disk to become thicker. It also appears that the thicker the disk, the sharper its ionization boundaries. The neutral He disk reaches down deeper than the hydrogen disk in model D, but it is still truncated at $\sim$2 R_*.

6. Observed profiles

Observed profiles for a converged ASTAROTH model are calculated independently by an auxiliary routine (described in Busche & Hillier 2005). We also used a Monte-Carlo code (Hillier 1991) for polarization calculations, and to verify the results of the auxiliary routine. Below we discuss the properties of the observed Hα profile, which arises from the disk, and the C IV $\lambda\lambda$1550 doublet profile, which primarily arises in the polar wind. We also discuss similarities and differences between the computed lines, and those seen for our benchmark B[e] supergiant R 126, although we stress that this work is not a spectral analysis of this star. For the calculations presented in the following sections we generally adopted 10 km s^{-1} for the Doppler parameter of the intrinsic line absorption/emission profile. Because of the low velocities in the disk, the adopted Doppler parameter can have a substantial influence on the line profile shape, and model profiles calculated with Sobolev approximation are significantly different. Furthermore, as the azimuthal velocities are zero in our models, the profiles are not rotationally broadened.

6.1. H Line profiles

The shape of the Hα lines in Fig. 6 are very sensitive to the observer's viewing inclination (i). Depending on the model either a single or double emission peak is seen; sometimes the emission peaks are well resolved, while at other times they blend into a continuous emission feature. For $i = 0$, the half-widths at the line base (HWLB) are 30−50 km s^{-1} which is slightly larger than V_∞ in the equatorial plane (20 km s^{-1}). Very weak wings, arising from emission in the wind outside of the equatorial latitudes, is also present. At higher inclinations the profiles are broader, and generally the emission is red-shifted. The red-shifted peak is always stronger than the blue-shifted peak, a characteristic feature often seen in real sgB[e] observations (see e.g., Zickgraf et al. 1985, 1986).

The double-peak profiles arise from optical depth effects in our simulations, and are not the result of rotation. The keys to understanding the double-peak profile are (1) that Hα is optically thick at the line center in all four models, and hence photons generally escape in the line wings where $\tau \sim 1$, and (2) that the Doppler velocity is comparable to the disk outflow velocity. Let's consider a spherical model with an extended atmosphere but no velocity field. In general, the source function will decrease with radius, and thus the maximum of the line source function, along a line of sight parallel to z-axis, will be in the xy plane. Optical depth unity will occur in the xy plane at two wavelengths, symmetrically located about line center. This will produce a distinct double-peaked profile with, in the absence of a velocity field, both peaks being of equal strength. However, when a velocity field is present, the red peak will be stronger than the blue. Photons emitted on the red side only see material moving away, and never come into resonance. On the other hand, photons emitted in the blue side must traverse material that is resonant with it, thus reducing the line intensity. The separation of the two peaks depends on the line width, and the overall profile and equivalent width is very sensitive to the adopted Doppler and wind velocities. When the wind velocity is much larger than the Doppler velocity we see a classic wind emission line with an optical-dependent redshift of 1 to 3 Doppler widths. As apparent from the above discussion, the blue/red peak asymmetry is not a specific feature of 2D models and also works for spherical envelopes, provided that the line is optically thick and the Doppler and flow velocities are comparable.

The shape of the pole-on viewed Hα in our model A is very similar to that seen in the spectra of R 126 (see Fig. 3 of Zickgraf et al. 1985). However, the simulated profile lacks the broad wings of the observations and is a factor of $\sim$10 weaker than it should be. This indicates that the density is much lower in Model A than it is in the envelope of R 126, and highlights the importance of frequency redistribution in electron scattering (the profiles in Fig. 6 were calculated ignoring electron-scattered line photons). The higher mass-loss rate in models C and D increases the equivalent width (it still falls short by a factor of $\sim$4, except at $i = 90°$), but the profiles now are very different from that of R 126. The very strong absorption around and blueward of the line center is not observed. This central absorption is very prominent for models B, C, D, and may indicate that hydrogen is more neutral in the line forming region of these models than it is around R 126.

Table 3 lists the equivalent widths (EW), the continuum levels across Hα, the total intensities arising in the Hα profiles (line

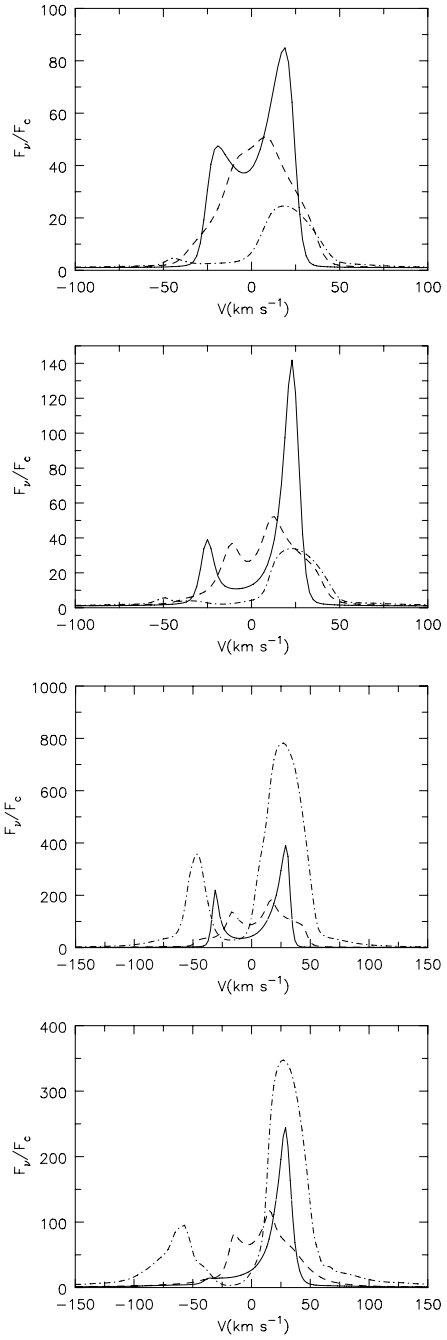

Fig. 6. Simulated observations of Hα for models A, B, C, and D (*top to bottom*). There are three viewing angles, $i = 0°$ (pole-on, solid line), 45° (dashed line), and 90° (edge-on, dash-dotted line). Note that all profiles are rectified.

fluxes), and the Hα to Hβ line flux ratios. The equivalent width varies with viewing angle, although the variation is weak for low to moderate inclinations. The continuum flux also varies with inclination angle. In models D and C the variation in continuum flux is large (the continuum is ∼10× smaller for the $i = 90°$ model than it is for $i = 45°$), and this causes the *EW* to be higher for the $i = 90°$ models, despite the lower line flux.

In modeling of O stars, LBVs, and W-R stars simple scaling laws can provide valuable insights into wind spectra, and greatly facilitate modeling through a reduction in the parameter space that needs to be explored. For W-R stars, Schmutz et al. (1989) found that models with the same effective temperature, and the same "optical depth invariant" parameter, $Q = \frac{\dot{M}}{(v_\infty R_*)^{1.5}}$, showed similar spectra. The same invariant also holds for recombination dominant transitions in O stars (Puls et al. 1996; de Koter et al. 1998). With the added complexity of 2D models, the identification of useful invariants is not so easy.

Table 3. Hα equivalent widths and line fluxes.

Model	i [I]	F_c [II]	EW (Å)	$F_l = EW \times F_c$	$\frac{F_l(H\alpha)}{F_l(H\beta)}$
A					
	0°	1060	61	64681	3.8
	45°	870	53	45736	3.8
	90°	384	21	8198	5.3
B					
	0°	754	54	40754	4.3
	45°	615	49	30320	4.4
	90°	267	30	8013	7.1
C					
	0°	3177	195	618689	5.7
	45°	2263	204	461810	5.7
	90°	107	873	93375	6.4
D					
	0°	1725	116	200859	6.4
	45°	1195	134	160345	6.6
	90°	134	392	52511	7.1

Note that the values (except the ratios) in this table are rounded up to the closest integers! [I]: Viewing angle, $i = 0°$ (pole-on), 45°, 90° (edge-on). [II]: Continuum intensity across Hα (in Jansky). Constant to 1−2%.

The extra difficulty of the 2D models is apparent from Table 3. First, continuum fluxes, line fluxes, and line *EW*s vary with the observer's inclination. Thus knowing the observer's inclination is crucial if meaningful envelope parameters are to be derived from the spectra. It is also apparent that for B[e] stars ionization effects are important, even for hydrogen. Models C and D, for example, have identical *Qs* but different *EW*s and line fluxes. Another complexity, not seen in W-R models, is that the *EW* and line-flux of Hα depends on the adopted Doppler velocity. When spectra for the very same models but with $V_{\rm turb} = 5$ km s^{-1} were calculated (not shown), the *EW*s and line fluxes decreased by ∼40%. The Hα to Hβ ratio, on the other hand, was not affected by the lower turbulent velocity.

To fully explore the effects of parameters on the observables is beyond the scope of this paper but simple trends can already be identified. It is striking, for example, that the ratio of the continuum intensities for $i = 45°$ and 0°, especially in models C and D, is close to $\cos(45°) = 0.71$ which is also the ratio of the projected area of a disk to its total area when tilted by 45°. One would expect such ratios if a substantial portion of the continuum around Hα formed in the transition region between the polar wind and the dense disk. The visible area of this disk "surface" would then control the continuum level. Furthermore, most of the Hα emission has to originate from the equatorial region since many of its characteristics cannot be explained in the context of a nearly spherical polar wind; e. g., its sensitivity to the observer's inclination angle. Simulations with CMFGEN (performed by the authors) also showed that one would need extreme stellar parameters to reproduce observed sgB[e] features in spherical models. Mass-loss rates in excess of 10^{-4} $M_\odot$ yr^{-1} and $v_\infty \leq 200$ km s^{-1} are required to match the observed linewidth and *EW* (∼900 Å, Zickgraf et al. 1985) for R 126.

It is more complicated to understand the spectra when the disk is viewed edge on. At $i = 90°$ the continuum is very low because the stellar radiation is seen through the dense equatorial

disk and the projected area of the disk is small. The very large *EW*s for $i = 90°$ viewing angle (see Table 3) are principally the result of the disproportionately low continuum; for high inclination angles the continuum weakens more with inclination angle than does the Hα emission. Since the continuum is low at every wavelength, these stars may appear unusually faint, and thus their luminosities and mass are underestimated.

A further important feature of the Hα emission is its $T_{\rm eff}$ dependence which mainly affects the absorption at and blueward of the line center. The lower the effective temperature is the stronger the absorption (see, for example, the difference between models B and A in Fig. 6). This is also apparent on the lower equivalent widths for models B or D relative to their respective high $T_{\rm eff}$ counterparts. It is not surprising that the hydrogen in these models is also less ionized and excited (relative to the models with higher $T_{\rm eff}$) which is clearly shown by the Hα to Hβ flux ratios listed in Table 3. The larger population in the low-lying states can also increase the self-absorption in the Balmer lines; hence it can explain the stronger absorption in models B and D.

6.2. C IV profile

The C IV doublet profile, for models A, B, C, and D, and for $i = 0°$, 45°, and 90° is shown in Fig. 7. A striking feature of the observed profiles in all models is the lack of red-shifted emission at pole-on and intermediate viewing angles (i.e., $i = 0°$ and 45°). This is also one of the notable features in the International Ultraviolet Explorer (IUE) observations of R 126 (Fig. 5 in Zickgraf et al. 1985).

The behavior of C IV is the exact opposite of what we saw in Hα. C IV is mainly in absorption formed in the polar wind, and shows little sensitivity to the viewing angle (at least until very nearly edge-on view). This is because the polar wind occupies a large solid angle around the star and it is also nearly spherical. A viewing angle of 0° or 45° makes little difference, apart from the position of the blue absorption edge. The role of the dense equatorial region in the formation of the C IV lines is to block the emission from the far side of the envelope. The profiles in Fig. 7 are also very sensitive to the effective temperature of the models. The absorption is much weaker for the lower $T_{\rm eff}$ models (B and D) than for their high temperature counterparts (A and C).

The edge-on viewed spectra in Fig. 7 are again complex. There is always a broad and strong emission component, the signature of the polar wind. They appear to be very strong in the rectified spectra only because they are seen against a very weak continuum. In three of the predicted profiles, doublet absorption components can also be seen. Their strength and shape is highly model dependent, and presumably arises from "disk" absorption of both line and continuum photons. The C IV profiles potentially offer an opportunity to constrain the thickness of the equatorial disk if the star is viewed nearly edge-on.

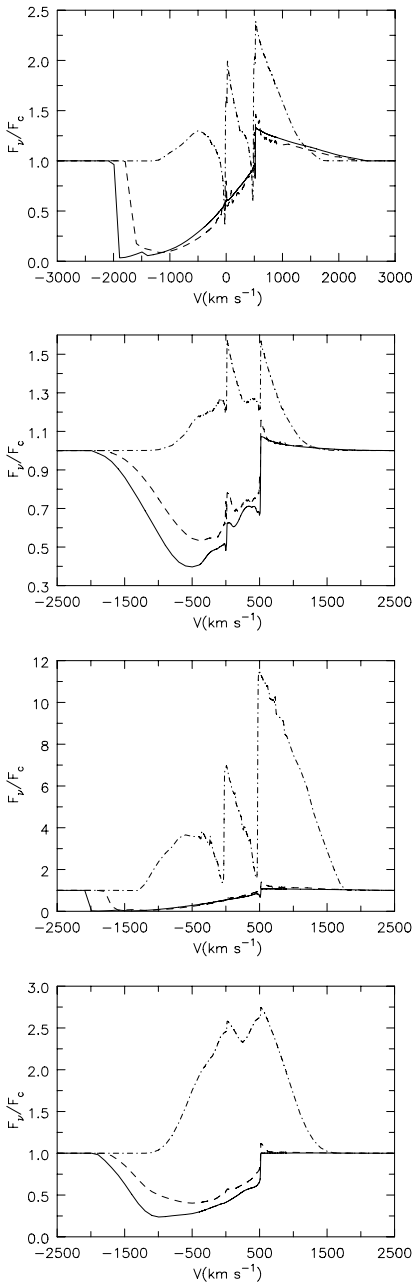

Fig. 7. Same as Fig. 6 but for C IV $\lambda\lambda$1550. Note that the velocity scale is centered on the doublet line with shorter wavelength.

7. Discussion

Obviously the substantial discrepancy between our ionization results and those of Kraus & Lamers (2003) needs an explanation. We think that the nebular approximation used by Kraus & Lamers (2003), is the reason for the differing results. In the nebular approximation it is assumed that all recombination to $n > 1$ levels of hydrogen will cascade down to level n=1 and the photo-ionizations from the $n > 1$ levels are completely negligible. In dense envelopes this is unlikely to be the case, as has been seen in studies of LBVs, W-R, and O stars. Drew (1985) studied P Cygni, an LBV with a mass-loss rate and luminosity similar to those of our models, and found that photo-ionization from the $n > 1$ states were crucial in determining the hydrogen ionization level. Similarly, Pauldrach (1987) recognized that ionization from excited states shifts the ionization level of elements higher in the wind of ζ Pup (O4f), and Hillier et al. (1983) and Hillier (1987) found that ionization from the $n = 2$ state of He was crucial in maintaining the He ionization balance in WR winds.

During a CMFGEN or ASTAROTH simulation, the radiative recombination to and photo-ionization from all included levels can be monitored, so their importance can be easily assessed. Figure 8 shows the ratio of the total photo-ionization from the excited states of hydrogen to the total recombination to the same levels for both CMFGEN and ASTAROTH models. For the nebular approximation to be valid, the ratios in Fig. 8 need to be

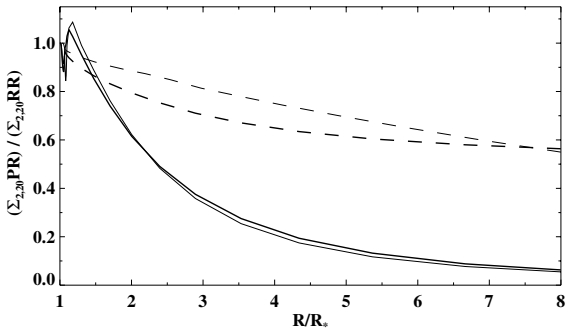

Fig. 8. The ratio of the total H photo-ionization (PR) from levels with $n > 1$ to the total recombination (RR) to levels with $n > 1$ for the pole (solid line) and equator (dashed line) of model A. The thick lines are for ASTAROTH (the actual 2D model) and the thin curves are the CMFGEN results (spherical models created for the given latitude).

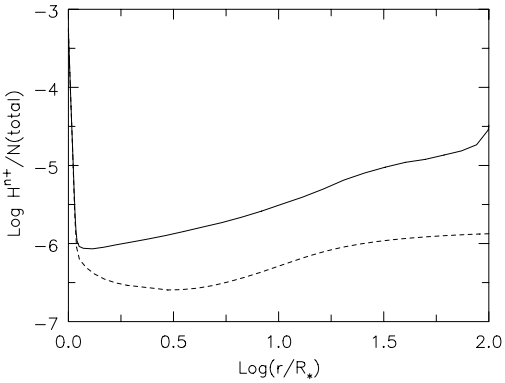

Fig. 9. The neutral hydrogen fraction as a function of radius in a spherical CMFGEN model created from the equatorial region of model A (dashed line); and in the actual equatorial region of our model A (solid line).

very small. However, the figure shows the ratios are significant, especially for the equatorial regions; therefore, we can conclude that the nebular approximation is not valid in the inner envelopes of these models. Ionization from the first few excited levels is extremely important, especially in the disk.

To simulate the nebular approximation with ASTAROTH is not trivial. One needs to shut down the photo-ionization terms from excited states in the less dense regions, but needs to keep them in the hydrostatic photosphere to recover LTE. Nevertheless, we experimented with spherical ASTAROTH models of the equatorial region of model A. To do this, we had to alter a few features of ASTAROTH. First, the inner boundary condition was changed from the diffusion approximation to a black-body function with $T_{\rm eff}$ = 22 500 K. With this modification the inner hydrostatic envelope could be omitted and the radiative transition rates could be "safely" modified to simulate the nebular approximation. When we ran the above simulations (equatorial region of model A) with this version of the code, hydrogen became neutral down to ~1.1 R_* with a negligible amount of H II. These experiments, therefore, fully supported the notion that ionization from higher levels is crucial in determining the hydrogen ionization levels in sgB[e] winds.

Despite the fact that hydrogen is ionized in most of our models, our simulations also prove that predominantly neutral material can exist around sgB[e] stars. In model D, for example, hydrogen has already recombined in the equatorial region. Furthermore, models B and C demonstrated that other species, like helium, can be neutral near the stellar surface even if hydrogen is ionized. It is a realistic expectation, therefore, that conditions suitable for molecule and dust formation may be found by more realistic ASTAROTH models. The task for follow-up studies is to map the parameter space (much more extended than the one for spherical models) and find their location. Our calculations also highlighted the complex nature of sgB[e] envelopes and the limitations of simple semi-analytic calculations. For detailed mapping of the parameter space, self-consistent numerical simulations are necessary.

Before we discuss our plans for the future, a few words about improving ASTAROTH and the sgB[e] models are warranted. One simplification in our sgB[e] models is the Sobolev approximation for the line transfer. At low latitudes the flow velocities were close to the ion thermal speed where the Sobolev approximation may no longer be accurate. We checked our results against CMFGEN models created from selected latitudes of the 2D models (e.g., pole or equator) that were using full line transfer. We saw no indication in these tests that departure from the Sobolev approximation would give a fundamentally different result. Note, that ASTAROTH and CMFGEN are very different codes and they use different solution techniques!

Figure 9 shows that the neutral hydrogen fraction is low in both the spherical non-Sobolev model and in the equator of the actual 2D calculation (model A). Such a comparison is not entirely valid, but it can reveal large inconsistencies if present. The results of CMFGEN and ASTAROTH, on the other hand, were in general agreement. The ionization level is approximately an order of magnitude lower in 2D since the radiation scatters off the dense disk preferentially toward the polar directions. This comparison also illustrates why modeling 2D problems with spherical codes, latitude by latitude, is not sufficient. Recreating this preferential scattering in a spherical context is impossible.

Another simplification is that the effects of rotation were neglected in the simulations presented here. This is a significant omission if sgB[e] stars are fast rotators, as thought. Kraus (2006) found important changes when they introduced these effects in their earlier models (Kraus & Lamers 2003) and we expect the same for our simulations. Rotation has four effects: First, rotation affects the dynamics of the circumstellar envelope, and the resultant line profiles. Second, rapid rotation causes gravity darkening such that the star is hotter at the poles than at the equator (von Zeipel 1924). Third, very rapid rotation causes the star to become oblate. Fourth, rotation alters the escape probabilities and thus the occupation numbers of various levels. The inclusion of the fourth and the first two effects into ASTAROTH is easy; the third is difficult.

We also anticipate significant changes when improving the atomic models. Iron is an especially important element to include because line-blanketing can seriously alter the radiation field, and hence influence the ionization of hydrogen and helium. Unfortunately, this is a time consuming task because iron has tens-of-thousands of lines, and in order to allow for blanketing the line transfer must be done in the CMF. An alternative is to introduce the effects of line-blanketing in an approximate manner (e.g., like in FASTWIND, Puls et al. 2005).

It is also very important to explore various dynamical concepts for sgB[e] envelopes and to include the non-radial velocity field. As mentioned in Sect. 1, the bi-stability mechanism is only one explanation for the observed bi-modal structure of the envelope. An important alternative is the Keplerian disk model which gained some support by recent hydrodynamical simulations (e.g., Madura & Owocki 2007). The problem with models based on the classical line driven wind

theory (Castor et al. 1975), like the bi-stability model, is that accelerating the large mass in the equatorial regions requires multiple scattering which is difficult to maintain if the photons can easily escape in the polar directions. This is the very same effect that allowed lower hydrogen ionization in 2D than in the corresponding spherical models (see Fig. 9). Furthermore, in hydrodynamical simulation of stars that are not close to the Eddington limit (Owocki et al. 1998), the enhanced flux at the pole of a rapidly rotating star tends to create a bipolar outflow rather than an equatorial disk.

In follow-up studies, we intend to improve ASTAROTH and will perform spectral analysis of specific sgB[e] stars. First, we plan to introduce non-radial velocities and the effect of rotation. We will also use a more realistic atomic model. The inclusion of iron blanketing is not trivial (primarily because of computational effort), so we will first concentrate on a realistic H, He, C, N, and O models. With these improvements we will undertake a spectroscopic analysis of R 126, and will use the well-observed sample of LMC/SMC sgB[e] stars (Zickgraf et al. 1985, 1986, 1992, 1996) to fully explore the allowed parameter ranges of the different sgB[e] models (Keplerian disk, bi-stability, etc.) and look for observable differences.

8. Summary

We performed numerical calculations of hydrogen and helium ionization in sgB[e] envelopes with ASTAROTH, our newly developed 2D stellar atmosphere code, and explored the effect of mass-loss and $T_{\rm eff}$ by sampling the upper end of the sgB[e] parameter range. We also presented theoretical profiles for Hα and the C IV $\lambda\lambda$1550 doublet and examined their behavior for different viewing angles, and as a function of the adopted stellar and envelope parameters. Our work yielded the following results:

1. We found that it is much harder to form neutral hydrogen in these sgB[e] envelopes than suggested by previous studies. The reason for the discrepancy is the nebular approximation used by the earlier studies; our calculation shows that ionization from excited states of hydrogen is very important in the envelopes of sgB[e] stars and highlights the need for self-consistent numerical simulations to study these objects.
2. Of the four models considered, only one formed a neutral hydrogen disk. Even in this case the disk did not extend to the stellar surface – it was truncated at $\sim$2–3 R_*. A neutral hydrogen disk formed for the combination of high mass-loss ($>10^{-5}$ $M_\odot$ yr^{-1}) and low effective temperature ($T_{\rm eff}$ < 18 000 K).
3. An equatorial disk predominantly neutral in helium forms for all but the lowest mass-loss rates ($<10^{-6}$ $M_\odot$ yr^{-1}).
4. The polar regions remain highly-ionized (e.g., C IV) in all models.
5. The simulated spectra showed many familiar features of sgB[e] observations, like the narrow double-peak Hα emission and UV resonance line P Cygni profiles without emission. We found that Hα forms mainly in the disk, and the strength of the continuum scales with the projected area of the disk-wind interface.

In the future we will include the effects of rotation (initially gravity darkening, non-radial velocities; later surface distortions) and improve our atomic model by including N, O, and more levels of C. We will further explore the parameter range, allowed for sgB[e] stars, by using the well-observed LMC/SMC sample of these stars. An obvious question to be addressed by these studies is – what is the structure of the disk (Keplerian, or dense outflow)?

Acknowledgements. This research was supported by NSF grant AST-0507328 and by Mexico CONACyT grant 42809 (L. N. Georgiev).

References

Bjorkman, J. E. 1998, in B[e] stars: Proceedings of the Paris workshop held 9–12 June, 1997., ed. A. M. Hubert, & C. Jaschek (Dordrecht; Boston: Kluwer Academic Publishers), 189
Bjorkman, J. E., & Cassinelli, J. P. 1993, ApJ, 409, 429
Busche, J. R., & Hillier, D. J. 2000, ApJ, 531, 1071
Busche, J. R., & Hillier, D. J. 2005, AJ, 129, 454
Castor, J., Abbott, D. C., & Klein, R. I. 1975, ApJ, 195, 157
Curé, M., Rial, D. F., & Cidale, L. 2005, A&A, 437, 929
Damineli, A., Kaufer, A., Wolf, B., et al. 2000, ApJ, 528, L101
de Koter, A., Heap, S. R., & Hubeny, I. 1998, ApJ, 509, 879
Drew, J. E. 1985, MNRAS, 217, 867
Georgiev, L. N., Hillier, D. J., & Zsargó, J. 2006, A&A, 458, 597
Groh, J. H., Hillier, D. J., & Damineli, A. 2006, ApJ, 638, L33
Hillier, D. J. 1987, ApJS, 63, 947
Hillier, D. J. 1991, A&A, 247, 455
Hillier, D. J. & Miller, D. L. 1998, ApJ, 496, 407
Hillier, D. J., Jones, T. J., & Hyland, A. R. 1983, ApJ, 271, 221
Humphreys, R. M., & Davidson, K. 1979, ApJ, 232, 409
Humphreys, R. M., & Davidson, K. 1984, Science, 223, 243
Kraus, M. 2006, A&A, 456, 151
Kraus, M., & Lamers, H. J. G. L. M. 2003, A&A, 405, 165
Kraus, M., Borges Fernandes, M., & de Arajo, F. X. 2007, A&A, 463, 627
Kunasz, P., & Auer, L. H. 1988, J. Quant. Spectrosc. Radiat. Transfer, 39, 67
Kurucz, R. L. 1979, ApJS, 40, 1
Lamers, H. J. G. L. M., & Pauldrach, A. W. A. 1991, A&A, 244, L5
Lamers, H. J. G. L. M., Zickgraf, F.-J., de Winter, D., Houziaux, L., & Zorec, J. 1998, A&A, 340, 117
Madura, T. I., & Owocki, S. P. 2007, ApJ, in press [arXiv:astro-ph/0702007]
Magalhaes, A. M. 1992, ApJ, 398, 286
Martin, J. C., Davidson, K., Humphreys, R. M., Hillier, D. J., & Ishibashi, K. 2006, ApJ, 640, 474
Melgarejo, R., Magalhaes, A. M., Carciofi, A. C., & Rodrigues, C. V. 2001, A&A, 377, 581
Mihalas, D., Auer, L. H., & Mihalas, B. R. 1978, ApJ, 220, 1001
Miroshnichenko, A. S., Bjorkman, K. S., Grosso, M., et al. 2005, A&A, 436, 653
Nielsen, K. E., Corcoran, M. F., Gull, T. R., et al. 2007, ApJ, in press [arXiv:astro-ph/0701632]
Oudmaijer, R. D., Proga, D., Drew, J. E., & de Winter, D. 1998, MNRAS, 300, 170
Owocki, S. P., & ud-Doula, A. 2004, ApJ, 600, 1004
Owocki, S. P., Gayley, K. G., & Cranmer, S. R. 1998, in Boulder-Munich II.: Properties of Hot, Luminous Stars, ed. I. D. Howarth, ASP Conf. Ser., 131, 237
Pauldrach, A. W. A. 1987, A&A, 183, 295
Pauldrach, A. W. A., & Puls, J. 1990, A&A, 237, 409
Pelupessy, I., Lamers, H. J. G. L. M., & Vink, J. S. 2000, A&A, 359, 695
Poeckert, R., & Marlborough, J. M. 1978a, ApJ, 220, 940
Poeckert, R., & Marlborough, J. M. 1978b, ApJS, 38, 229
Porter, J. M. 2003, A&A, 398, 631
Puls, J., Kudritzki, R.-P., Herrero, A., et al. 1996, A&A, 305, 171
Puls, J., Urbaneja, M. A., Venero, R., et al. 2005, A&A, 435, 669
Quirrenbach, A., Bjorkman, K. S., Bjorkman, J. E., et al. 1997, ApJ, 479, 477
Rybicki, G. B., & Hummer, D. G. 1991, A&A, 245, 171
Rybicki, G. B., & Hummer, D. G. 1992, A&A, 262, 209
Schmutz, W., Hamann, W.-R., & Wessolowski, U. 1989, A&A, 210, 236
Schulte-Ladbeck, R. E. 1998, in B[e] stars: Proceedings of the Paris workshop held 9–12 June, 1997, ed. A. M. Hubert, & C. Jaschek (Dordrecht; Boston: Kluwer Academic Publishers), 253
Stee, P., de Araújo, F. X., Vakili, F., et al. 1995, A&A, 300, 219
ud-Doula, A., & Owocki, S. P. 2002, ApJ, 576, 413
Vink, J. S., de Koter, A., & Lamers, H. J. G. L. M. 1999, A&A, 350, 191
von Zeipel, H. 1924, MNRAS, 84, 665
Zickgraf, F. J. 1998, in B[e] stars: Proceedings of the Paris workshop held 9–12 June, 1997, ed. A. M. Hubert, & C. Jaschek (Dordrecht; Boston: Kluwer Academic Publishers), 1
Zickgraf, F.-J., Wolf, B., Stahl, O., & Leitherer, C.and Klare, G. 1985, A&A, 143, 421
Zickgraf, F.-J., Wolf, B., Stahl, O., Leitherer, C., & Appenzeller, I. 1986, A&A, 163, 119
Zickgraf, F.-J., Stahl, O., & Wolf, B. 1992, A&A, 260, 205
Zickgraf, F.-J., Humpreys, R. M., Lamers, H., et al. 1996, A&A, 315, 510
Zsargó, J., Hillier, D. J., & Georgiev, L. N. 2006, A&A, 447, 1093